Article

Optimization of Sb$_2$S$_3$ Nanocrystal Concentrations in P$_3$HT: PCBM Layers to Improve the Performance of Polymer Solar Cells

E. M. Mkawi [1,2,*], Y. Al-Hadeethi [2], R. S. Bazuhair [3], A. S. Yousef [3], E. Shalaan [2], B. Arkook [2], A. M. Abdeldaiem [2], Rahma Almalki [2] and E. Bekyarova [4]

[1] K.A.CARE Energy Research and Innovation Center, King Abdulaziz University, Jeddah 21589, Saudi Arabia
[2] Department of Physics, Faculty of Science, King Abdulaziz University, Jeddah 21589, Saudi Arabia; yalhadeethi@kau.edu.sa (Y.A.-H.); eshalan@kau.edu.sa (E.S.); barkook@kau.edu.sa (B.A.); abdeldaiem@hotmail.com (A.M.A.); ralmalki0259@stu.kau.edu.sa (R.A.)
[3] Department of Drawing and Art, College of Art and Design, Jeddah University, Jeddah 23345, Saudi Arabia; Rehabsyb@gmail.com (R.S.B.); Asyuosef@uj.edu.sa (A.S.Y.)
[4] Department of Chemistry, University of California at Riverside, Riverside, CA 92521, USA; elena.bekyarova@ucr.edu
* Correspondence: moizmerghni@yahoo.com.my

Abstract: In this study, polymer solar cells were synthesized by adding Sb$_2$S$_3$ nanocrystals (NCs) to thin blended films with polymer poly(3-hexylthiophene)(P$_3$HT) and [6,6]-phenyl-C61-butyric-acid-methyl-ester (PCBM) as the p-type material prepared via the spin-coating method. The purpose of this study is to investigate the dependence of polymer solar cells' performance on the concentration of Sb$_2$S$_3$ nanocrystals. The effect of the Sb$_2$S$_3$ nanocrystal concentrations (0.01, 0.02, 0.03, and 0.04 mg/mL) in the polymer's active layer was determined using different characterization techniques. X-ray diffraction (XRD) displayed doped ratio dependences of P$_3$HT crystallite orientations of P$_3$HT crystallites inside a block polymer film. Introducing Sb$_2$S$_3$ NCs increased the light harvesting and regulated the energy levels, improving the electronic parameters. Considerable photoluminescence quenching was observed due to additional excited electron pathways through the Sb$_2$S$_3$ NCs. A UV–visible absorption spectra measurement showed the relationship between the optoelectronic properties and improved surface morphology, and this enhancement was detected by a red shift in the absorption spectrum. The absorber layer's doping concentration played a definitive role in improving the device's performance. Using a 0.04 mg/mL doping concentration, a solar cell device with a glass /ITO/PEDOT:PSS/P$_3$HT-PCBM: Sb$_2$S$_3$:NC/MoO$_3$/Ag structure achieved a maximum power conversion efficiency of 2.72%. These Sb$_2$S$_3$ NCs obtained by solvothermal fabrication blended with a P$_3$HT: PCBM polymer, would pave the way for a more effective design of organic photovoltaic devices.

Keywords: solar cells; Sb$_2$S$_3$ nanocrystals; P$_3$HT: PCBM polymer

1. Introduction

Solar cell-based organic semiconductors have many advantages, such as low cost, lightweight, flexibility, low material consumption, easy fabrication, and large area production [1,2].The organic photovoltaic (PV) solar cells continue to find a widespread application, in particularly in the following areas: solar farms, remote locations, powering stand-alone devices, powering earth-orbiting satellites and space stations, building structures such as windows and roof tiles, martial utilizations, and in aviation to power aircrafts at high altitudes. Polymers are often used as adjustment additives in dye-sensitized solar cells to provide a desirably resilient substrate, a frame structure of the semi solid state electrolytes, in addition to the pore/film formation in photoanode films. Moreover, polymers are added to enhance a solar cell device's performance, such as reinforcing the processes of

crystallization and nucleation in the perovskite solar cell films. Polymers are applied as buffer layers or donor layers to improve a device's efficiency. Polymers are also applied as electron transmitters, hole transmission materials, as well as interfacial layers, which improve the carrier separation efficacy and minimize the recombination.

Poly(3-hexylthiophene) and [6,6]-phenyl-C61-butyric acid methyl ester, P_3HT-PCBM blends are promising organic polymers that have been used as photovoltaic materials [3]. They are considered to be a promising fullerene derivative-based donor-acceptor electron material for organic solar cells. PCBM polymers are fullerene derivatives as electron acceptors for organic photovoltaics because of their high electron mobility. P_3HT is a member of the polythiophene-conducting polymer family, in which excitation of the π-orbit electron in P_3HT produces photovoltaic effects in the blend [4]. The blend's energy gap is approximately 1.8 eV and should exhibit a high absorption wavelength around 650 nm.

The lifetimes of organic solar cells remain short due to the degradation mechanisms that occur in organic compounds and oxidation of the electrode materials. However, strictly controlling this morphology is severely limited, which will lead to charge carrier recombinations because of incomplete pathways for both types of charge carriers if the films are thicker than 150 nm [5]. The donor–acceptor morphology can be controlled using the metal sulfide geometry, which can create good percolation pathways. Using ordered nanostructures such as nanocrystals or nanoparticles is promising for controlling the final structure, as electrons can be transported along one-dimensional structures over many micrometers, which reduces carrier recombinations [5,6]. P_3HT forms ordered microcrystalline structures in the solid state. The presence of ordered crystalline structures in solid thin films helps to obtain high device performance because of the improved hole mobility from stacking thiophene rings and forms an enhanced light absorption with ordered structures in longer wavelength regions. Thus, incorporating inorganic and nanostructure semiconductors has several advantages, such as high electron mobility and physical and chemical stability [7,8]. However, some disadvantages are present, such as the formation of large aggregates of nanostructures, which may be effective in active layer morphology charge mobility.

Many nanostructure materials, such as PbS, ZnO, CdS, TiO_2, and Sb_2S_3, have been used in polymer solar cells due to their high electron mobility. Sb_2S_3 is a semiconductor material with a unique one-dimensional crystal structure, higher stability in air, and diverse Sb-S bond lengths. Sb_2S_3 is a non-toxic, abundant material with an indirect band gap of 1.7–1.8 eV, an absorption coefficient higher than 104 cm^{-1}, and high electric conductivity, which make it a suitable material for use as light harvesters in photovoltaic applications. Sb_2S_3 nanocrystals may provide a significant contribution to the absorption in polymer/Sb_2S_3 nanocrystal solar cells [9–11]. In a study incorporating semiconductor P_3HT:PCBM nanoparticles, Zhao et al. [12] showed that adding PbS quantum dots (QDs) to P_3HT changed the chemical structure, which improved the active layer via an optimized phase separation and increased carrier transfers. Kim et al. [13] reported a PCE of approximately 2.98% by combining various concentrations of ZnO nanoparticles grown using the hydrothermal method with a P_3HT: PCBM blend. They suggested that the improved charge balance and performance may have been due to reducing the charge recombinations and oxygen vacancies from the cathodes.

In this study, we report the fabrication of Sb_2S_3 NCs for their application in one of the most efficient organic solar cells consisting of PTB7: PCBM organic photovoltaic blends. To the best of our knowledge, the effect of the Sb_2S_3 NC additive on the properties of P_3HT:PCBM blend solar cells that employ solid hole conductors has not been investigated. High-quality Sb_2S_3NPs were synthesized using solvothermal techniques at a hydrothermal temperature of 180 °C. The effect of different Sb_2S_3 NC concentrations incorporated with PTB7: PCBM was investigated in detail using different characterization methods. The experimental results indicated that the self-assembly of the PTB7: PCBM Sb_2S_3 NC polymer and intermolecular orientation in the P_3HT crystallite was greatly influenced by Sb_2S_3 nanocrystal doping. By adding Sb_2S_3 NCs, the electrons and holes transfer in the polymer active layer enhanced our results, which led to an improved carrier separation efficiency

and a reduced recombination. The absorption spectra of the sample, after adding Sb_2S_3 NCs, was better attributed to the π-π* transitions. The Sb_2S_3NPs help to disperse the P3HT chains in a solution and promote transformation and, thus, improve the crystallization of P3HT (during film forming process) as well as the device's efficiency. The solar cell device in a structure glass/ITO/PEDOT:PSS/P_3HT: PCBM:Sb_2S_3:NCs/MoO_3/Ag achieved a maximum power conversion efficiency of 2.72% using an Sb_2S_3NC concentration of 0.04 mg/mL. Hence, Sb_2S_3NC-doped P3HT-PCBM thin films have great potential applications as active layers in solar cell devices and can be an efficient method to improve thin film properties.

2. Experiment

2.1. Sb_2S_3 Nanocrystals Fabrication

For the typical solvothermal fabrication of Sb_2S_3 nanocrystals, 0.2 mmol of $SbCl_3$ and 4 mmol of I-cystine were dissolved in 10mL of oleylamine. Then, 4 mmol of thiourea was dissolved in 10 mL of oleylamine in a separate beaker under stirring for 2 h. The antimony solution was dropped slowly into the latter solution under vigorous magnetic stirring. The mixed solutions were then transferred into a 50-milliliter Teflon-lined, stainless steel autoclave and placed in a tubular furnace at 180 °C for 24 h. The resulting precipitate was first centrifuged, and the black product was washed with ethyl alcohol and deionized water and dried at 70 °C for 5 h.

2.2. Device Fabrication

Indium tin oxide (ITO)-coated glass substrates, approximately 120 nm thick with a sheet resistance of around 15 Ω/sq and a 1.5×1.5 cm^2 device area were used as an anode contact in the organic solar cell device. Acetone or isopropanol were soaked in an ultrasonic bath for 5 min, followed by drying in an N_2-filled glove box. A PEDOT:PSS polymer was deposited at 3500 rpm for 50 s, using spin coating followed by annealing at 120 °C for 15 min in a furnace in air, resulting in a thickness of ∼60 nm. The PEDOT:PSS/ITO/glass substrates were moved to a nitrogen-supplied glove box and annealed again at 130 °C for 10 min to avoid humidity. The blended P_3HT and PCBM solution was prepared by dissolving the polymers in 1,2-dichlorobenzene with a ratio of 1:1 and 50 mg of each polymer. The mixed solutions were stirred at 60 °C overnight. The Sb_2S_3 nanocrystals were blended in the P_3HT: PCBM in a concentration range of 0.01, 0.02, 0.03, and 0.04 mg/mL. The P_3HT:PCBM:Sb_2S_3:NC nanocomposites were spin-coated on top of PEDOT:PSS layers at 1500 rpm for 40 s inside a glove box. The active layer's average thickness was 100–120 nm, and the spin-coated layer was annealed at 140 °C for 10 min in a nitrogen-filled glove box. A buffer layer, with approximately 20 nm of MoO_3, was deposited using RF spurting. The thick Ag electrode (70 nm) was thermally evaporated, and the active area was approximately 0.1 cm^2. The final device had the following structure: ITO/PEDOT:PSS/P_3HT:PCBM:Sb_2S_3:NCs/MoO_3/Ag. A schematic illustration of a typical device structure is shown in Figure 1.
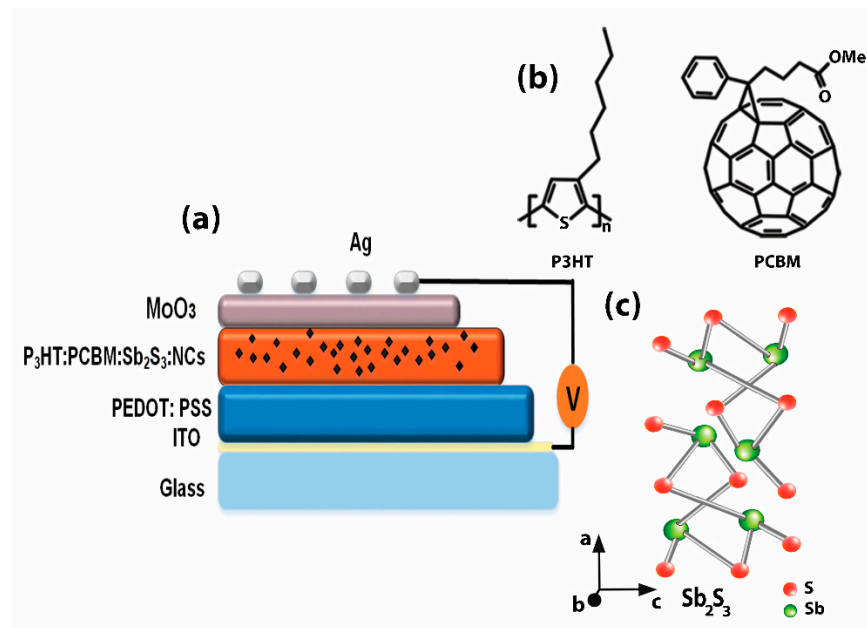
Figure 1. (**a**) Schematic configuration of the inverted polymer solar cell showing the glass/ITO/PEDOT:PSS/P$_3$HT:PCBM:Sb$_2$S$_3$:NCs/MoO$_3$/Ag layers and chemical structure of the (**b**) P$_3$HT, PCBM, and (**c**) Sb$_2$S$_3$ nanocrystals.

2.3. Characterization

The structural properties of the Sb$_2$S$_3$ nanocrystals and P$_3$HT:PCBM:Sb$_2$S$_3$ NCs were investigated using an X-ray diffractometer (MiniFlex, Rigaku, Tokyo, Japan) with monochromatic Cu Kα radiation (λ = 1.5405 Å). The UV–visible spectroscopy investigation was performed using a Varian Cary 100 spectrophotometer (Agilent Technologies, Santa Clara, California, USA). A transmission electron microscopy (TEM) analysis was obtained using a JEOL 2010F (JEOL 2010F field emission high resolution scanning/transmission electron microscope, Akishima, Tokyo, Japan) to examine the Sb$_2$S$_3$ nanocrystal's properties. Atomic force microscopy (AFM) measurements were performed on a standard Keysight 5500 scanning probe microscope (Keysight Technologies Fountain grove Parkway, Santa Rosa, CA 95403) in the intermittent contact mode in air. The photoluminescence spectra were collected using a Hitachi F-7000 spectrometer (Hitachi F-7000 fluorescence spectrophotometer, Toranomo, Minato-ku, Tokyo, Japan) equipped with a red-sensitive detector. The Fourier-transform infrared spectroscopy (FTIR) of the polymer/NC blended films was investigated using a Nicolet 8700 (Thermo Fisher Scientific, Madison, WI, USA) spectrometer. Raman spectroscopy of the active layer was performed using a Renishaw inVia Raman microscope (Renishaw inVia Raman microscope, Gloucestershire, United Kingdom) (λ = 514 nm). The current density–voltage (J–V) characteristics of the polymer device were measured under AM 1.5 G and 100 mW cm^2 illumination using a Keithley 2400 (Keithley, Tektronix, Solon, Ohio, USA) for source measurement.

3. Results and Discussion

The crystal sizes and phase information on the Sb$_2$S$_3$ were confirmed using X-ray diffraction (XRD) patterns from the pure Sb$_2$S$_3$ nanocrystals prepared using the solvothermal method as shown in Figure 2a. All of the XRD patterns in Figure 2a present the stibnite structure of the Sb$_2$S$_3$ (JCPDS No. 42-1393). For example, the diffraction peaks at 2θ = 17.7, 24.4, 32.8, 35.1, 44.1, 54.3, and 46.4° corresponded to the (120), (130), (221), (301), and (511) orientations, respectively, with a preferred orientation along the (130) plane. The sharp and high-intensity peaks indicated that the product had high crystallinity. No peaks were associated with other phases, which indicated the sample's high purity. The lattice parameter identical to the orthorhombic type was a = 11.23 Å, b = 11.28 Å, and c = 3.83 Å. These

results agreed with previously reported studies of Sb_2S_3 materials [14,15]. The crystallite size of the Sb_2S_3 nanocrystals was 41 nm, as determined using the Scherrer formula [16].
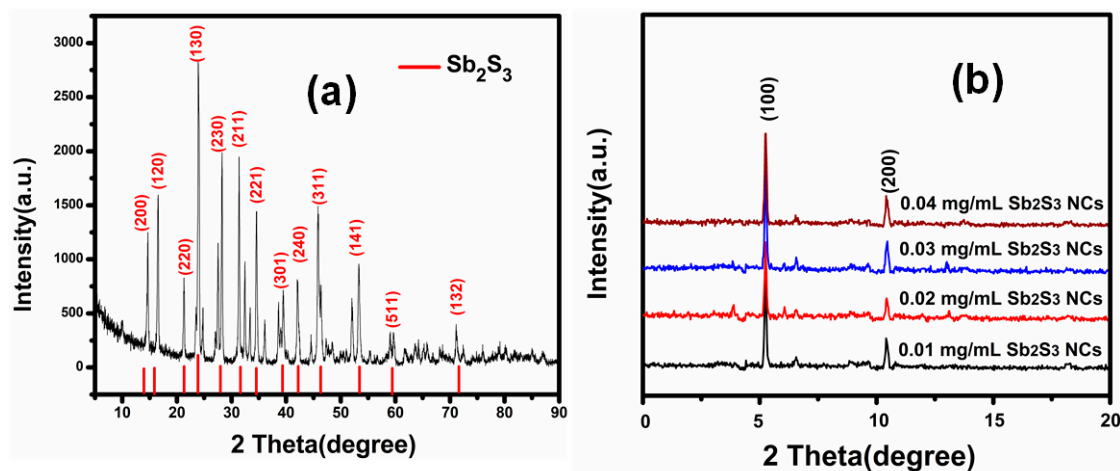

Figure 2. XRD diffraction of (**a**) pure Sb_2S_3 nanocrystals prepared using the solvothermal method (**b**) in P_3HT:PCBM:Sb_2S_3 NC blended films spin-coated with different Sb_2S_3 NC concentrations.

To assess the crystalline development of the P_3HT:PCBM: Sb_2S_3 NCs' active layer, the sample's XRD patterns were recorded. Figure 2b shows the XRD profiles of P_3HT:PCBM: Sb_2S_3 NC blended films spin-coated at 1500 rpm for 40 s. The XRD analysis was recorded in a narrow range ($2\theta = 3$–$10°$). The increase in the (100) peak intensity corresponding to P_3HT was observed at $2\theta = 5.4°$, which agreed with prior studies [17,18]. The diffraction peak located at $2\theta = 19°$ corresponded to crystalline PCBM [19]. The XRD (100) peaks shifted to lower angles, from 5.58 to 5.39°, as the dispersion degree increased. This shift (change in D spacing) indicated the improved diffusion of the PCBM into the P_3HT, decreasing the distance between them [20]. The diffraction peaks became narrower and sharper as the Sb_2S_3NCs' concentration increased, indicating an increase in the crystallinity, suggesting orderliness, and increasing the intermolecular π plane. The P_3HT:PCBM: Sb_2S_3 NCs' blend displayed a high crystallinity that improved regardless of the presence of fullerene. The growth of the P_3HT aggregate improved the chains' crystallinity and hole mobility, which resulted in positive J–V curves [21].

Raman spectroscopy in a range of 250 to 2500 cm^{-1} was used to investigate the molecules' irrational mode in the P_3HT:PCBM:Sb_2S_3 NC blended films. The Raman spectra of the P_3HT:PCBM: Sb_2S_3 NC blended films shown in Figure 3 features the vibration modes, as reported in previous studies, including the vibration spectra, and the stretching and bending modes with different relative intensities varying from high to low values. The amount of Sb_2S_3 NCs contributed to the changes in the peak intensity. The peaks at $\sim$578 to $\sim$782 cm^{-1} coincided with C-H out-of-phase bending [22]. As most studies of polymers suggested, the peak located at 728 cm^{-1} was related to rocking vibrations in the C-S-C thiophene ring of the P_3HT [22,23]. The peak found at $\sim$1086 cm^{-1} was not from the P_3HT molecules; therefore, this vibration peak may have corresponded to interactions of the P_3HT molecules and the Sb_2S_3 NCs. The peak located at $\sim$1378 cm^{-1} was associated with the asymmetric vibrations of C=C skeletal stretching deformation, and the peak appearing at$\sim$1518 cm^{-1} corresponded to stretching vibrations from the P_3HT, which agrees with a previous study [24]. A higher intensity peak at $\sim$1442 cm^{-1} was related to the high P_3HT structural order [25]. At this peak, the combined skeletal stretching of the complete chain, or at least a large part of it, was found. This mode was dominated by the inter-ring C-C stretching vibration mode and was the origin of the vibronic structure of the absorption and emission spectra [25,26]. The intensity of the $\sim$1442 cm^{-1} peak related to the phonon features was reduced due to the presence of the Sb_2S_3 NCs, suggesting an increased order in the blended system and enhanced conjugation lengths.
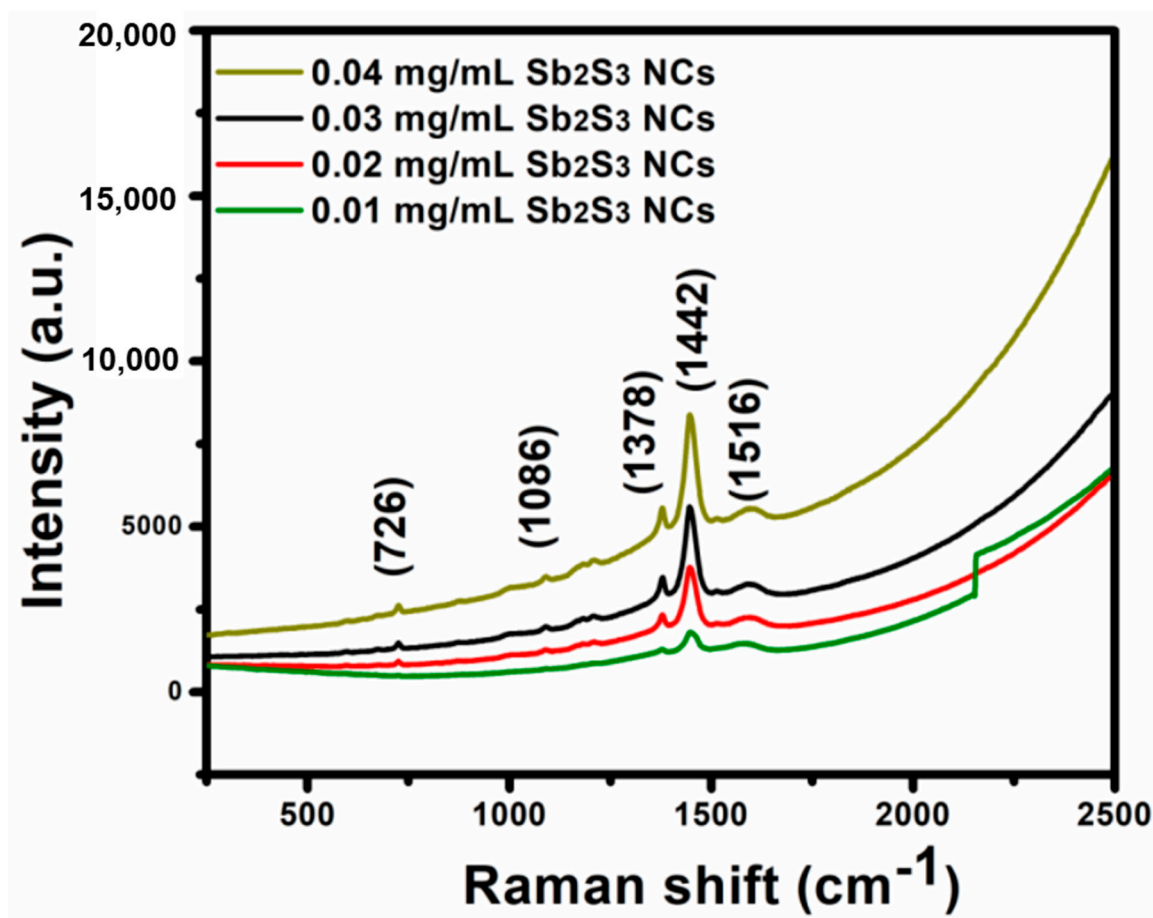
Figure 3. Raman spectra of theP$_3$HT:PCBM:Sb$_2$S$_3$ NC blended thin films prepared using spin coating.

To obtain accurate morphological and size information, TEM images and diffraction patterns were obtained for the sample. Figure 4a–c show TEM images of the Sb$_2$S$_3$ nanocrystals prepared using the solvothermal method at 230 °C. The typical TEM images shown in Figure 4a confirm that the morphology of the Sb$_2$S$_3$ was a nanocrystalline along the (001) direction with a diameter of approximately 100 nm. The selected area electron diffraction SAED images in Figure 4b show the sharp spots of the Sb$_2$S$_3$, where the diffraction spots indicate the fully crystalline nature of the Sb$_2$S$_3$NCs and the main diffraction plane matched with the standard XRD patterns shown in Figure 2. The high-resolution TEM (HRTEM) images are shown in Figure 4c and the lattice spacing of 0.32 nm agrees well with the (130) diffraction of the Sb$_2$S$_3$. The SAED images and corresponding HRTEM images demonstrated that the crystalline nature of the Sb$_2$S$_3$ NCs agreed with the XRD and Raman results.

The optical absorption spectra of the Sb$_2$S$_3$ nanocrystals recorded in a range of 200—800 nm is shown in Figure 5a. The Sb$_2$S$_3$ nanocrystals had high absorption coefficients above 5×10^4 cm^{-1} in a wavelength range of 350–750 nm. The strong absorption intensity was attributed to the good quality of the Sb$_2$S$_3$ nanocrystals. A large absorption coefficient is important for solar cell applications, which implies a high short-circuit current density. The energy gaps of the Sb$_2$S$_3$ NCs were calculated by plotting the $\alpha h\nu^{1/2}$ vs. $h\nu$ and extrapolating the linear portion of the curve to $\alpha h\nu = 0$, as shown in Figure 5a (insert). The optical bandgap (Eg) determined using the Tauc equation [27] was 1.79 eV.
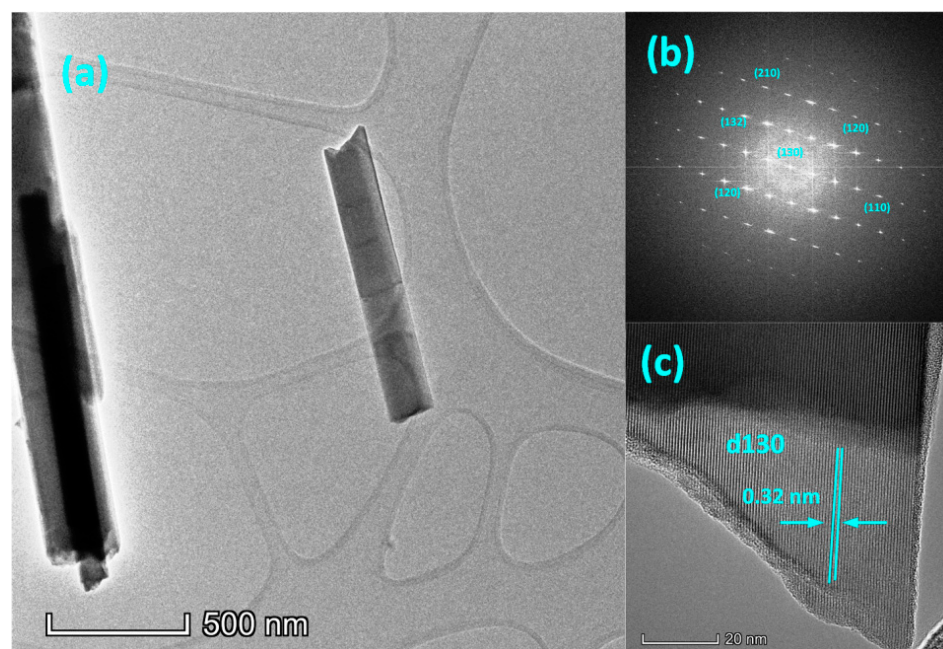
Figure 4. (**a**) TEM images of the Sb_2S_3 NCs. (**b**) Selective area electron diffraction (SAED). (**c**) High-resolution (HRTEM) image of the fabricated Sb_2S_3 NCs.

To investigate the photon-gathering ability of the P_3HT:PCBM:Sb_2S_3 NCs' active layer, UV–visible absorption spectra of the sample were recorded in a wavelength range of 300–800 nm. Figure 5b shows the UV–visible absorption spectra of the P_3HT:PCBM:Sb_2S_3 NC blended films prepared using different concentrations of Sb_2S_3 NCs (0.01, 0.02, 0.03, and 0.04 mg/mL). The absorption spectra in a range of 450–600 nm were attributed to the main P_3HT polymer. The absorption spectra of the P_3HT:PCBM:Sb_2S_3NCs' active layer showed an absorption peak of π-π* aggregate formation at a wavelength of 512 nm, with two small shoulders at 550 and 604 nm. The P_3HT polymer displayed an atypical absorption band at approximately 512 nm that was attributed to the π-π* transitions, this result is in good agreement with previous studies [28,29]. The π-π* band of the active layer showed a 3-nanometer red shift corresponding to the P_3HT polymer, suggesting more efficient π stacking. Sb_2S_3 NCs had absorption spectra below 550 nm in previous studies. Sb_2S_3 NC doping may have strongly contributed to the buffer absorbance within a 300–550 nm range. Doping resulted in a clear red shift of the optical absorption, mainly in the 512 nm band, which shifted from 500 to 512 nm. The red shift in the absorption band could be attributed to increasing the π electron delocalization, lowering the energy band of the π and π*, and improving the optical π-π* transitions [30,31]. The increase in the light-harvesting properties of the P_3HT:PCBM:Sb_2S_3 NC blend improved the photo-generated carriers and enhanced the charge transport due to the π-π interactions between the Sb_2S_3 NCs and the P_3HT molecules. The absorption strength was increased, along with the different concentrations, due to the improved polymer crystallinity. However, the improved absorption may have been due to the decreased film roughness, which affected the light scattering in the blended films, resulting in increased absorption in the active layer.

Figure 6 shows a schematic energy level diagram of the energy and charge transfer effects of the P_3HT:PCBM:Sb_2S_3 NC blend. There are the following three possible reasons for the electron movement in the P_3HT:PCBM:Sb_2S_3 NC system: electron transport from the P_3HT to the PCBM; electron transfer from the P_3HT to the Sb_2S_3 NCs; and electrons moving from the P_3HT to the Sb_2S_3 NCs, and then to the PCBM. In these cases, the electrons transformed into Ag, while the holes transformed out of the P_3HT to the ITO layer, which reduced the chances of carrier recombination. Thus, incorporating the Sb_2S_3 NCs with the polymer contributed to more photo-induced charge carrier separations/transfers that increased the photo-generated exciton dissociation [8,32]. The processes can occur

depending on the excitation energy. When excitons are formed upon light absorption in the Sb_2S_3 NCs, it is expected that the electrons will be transferred to PCBM and holes to P3HT. When excitations are generated in P3HT, we can predict from the energy levels that an electron transfer will occur toward the Sb_2S_3 NCs and/or PCBM [33]. To learn more about the processes occurring between the blend components, we investigated steady state and time-resolved PL.
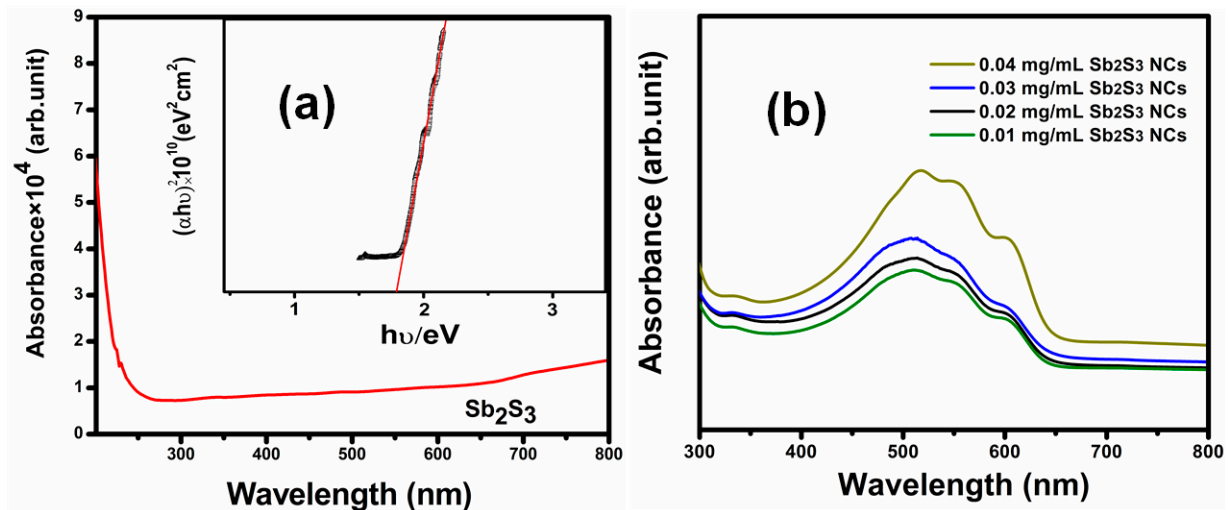

Figure 5. (**a**) UV–visible spectra absorption spectroscopy and band gap energy estimation of the Sb_2S_3 NCs (insert). (**b**) UV–visible spectra of theP$_3$HT:PCBM:Sb_2S_3 NC polymer fractions blended with different Sb_2S_3 NC concentrations.
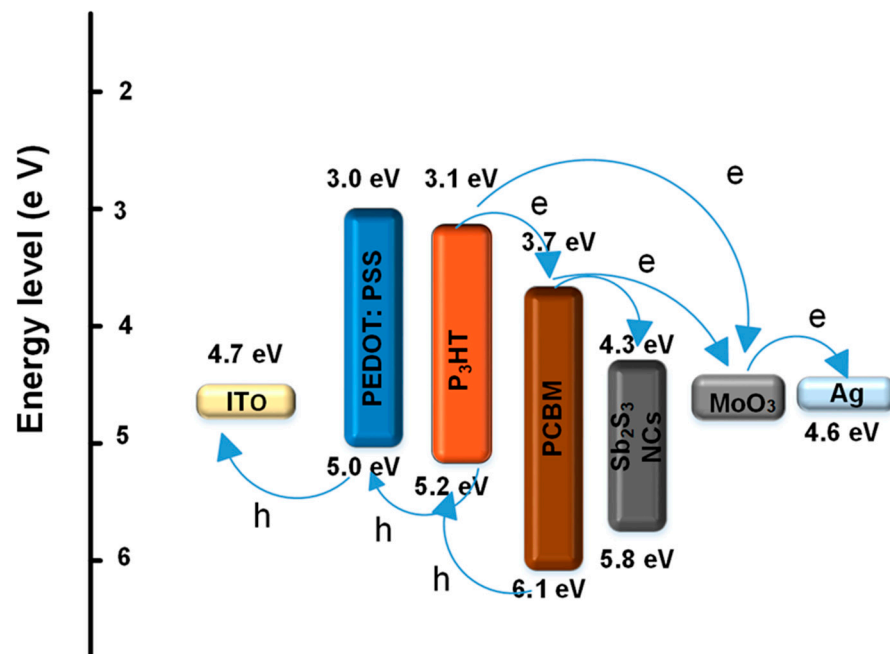

Figure 6. Energy band diagram and charge transfer effects of the P$_3$HT, PCBM, and Sb_2S_3 NCs.

To study the effect of the Sb_2S_3 NCs on the exciton dissociation, the PL spectra of the P$_3$HT:PCBM:Sb_2S_3 NC thin films with different concentrations of Sb_2S_3 NCs were investigated using a PL spectral system, as shown in Figure 7. The PL peak of the P$_3$HT:PCBM:Sb_2S_3 NCs was observed at 630 nm, in good agreement with previous studies for P$_3$HT:PCBM [34,35]. At higher Sb_2S_3 NC concentrations, the peaks become more intense and emission peaks at 635nm red-shifted to 639 nm, which may have been related

to band-to-band emission in the P_3HT, since it had a narrow band gap of approximately 1.9 eV.

The increased PL intensity indicated the improved phase separation size, which benefited the charge transport and collection. The size range of the P_3HT and PCBM exceeded the exciton diffusion length because of the increased phase separation between the PCBM and P_3HT after doping. A large increase in the PL intensity was observed, consistent with the increased diffusion of the PCBM in the P_3HT matrix, leading to increased carrier transfers [36]. Consequently, the exciton-dissociation efficiency decreased, while the PL efficiency increased. These results indicated that the energy and charge transfer occurred between the P_3HT, PCBM, and Sb_2S_3 NC material.
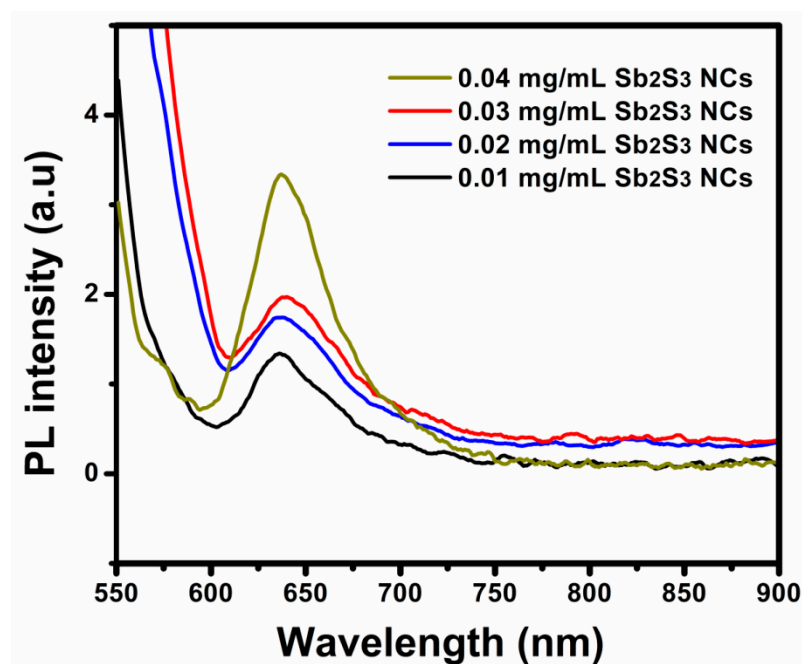

Figure 7. Photoluminescence spectra of the spin-coated P_3HT:PCBM:Sb_2S_3 NCs prepared using different Sb_2S_3 NC concentrations.

Atomic force microscopy (AFM) was used to investigate the tapping mode operation and phase distribution of the blends. Figure 8a–d shows AFM height images of the surface roughness and grain size of the P_3HT:PCBM:Sb_2S_3 NC thin films prepared with different Sb_2S_3 NC concentrations. The images show the network structures of self-organized P_3HT chains similar to the seed-like polymer chains reported in previous studies [37,38]. The bright areas (higher phases) in the phase images can be identified as P_3HT-rich regions, while the dark areas (lower phases) can be identified as PCBM-rich regions. The phase images of the active layer display a considerable variation in the phase segregation length scale. The size of the P_3HT area and PCBM domains, in a range of 24.3 to 59.27 nm, depended on the NC concentration. This indicated that two sequential polymer chains were separated within the exciton diffusion length, with PCBM nanoclusters established between the chains.

Evidently, the Sb_2S_3 NC acted as a compatibilizer and modified the average domain size of the PCBM by the intermolecular hydrogen bonds generated from the C-H-Os bonds; therefore, the active layer became smoother. The increase in the surface roughness could also have been due to the improved crystallinity of the P_3HT in the film. This occurred because of the decreased P_3HT aggregation size and increased number of P_3HT single chains. The P_3HT crystallization degree and effective phase blending had a major influence on the electron and hole mobility in the photovoltaic blend. The P_3HT crystallization degree and effective phase blending had a major influence on the electron and hole mobility, which enhanced the carrier recombination and reduced the recombination layer of the solar cell

device. As reported in prior studies, a high-efficiency photovoltage has a high surface roughness in P$_3$HT:PCBM blended thin films [39].
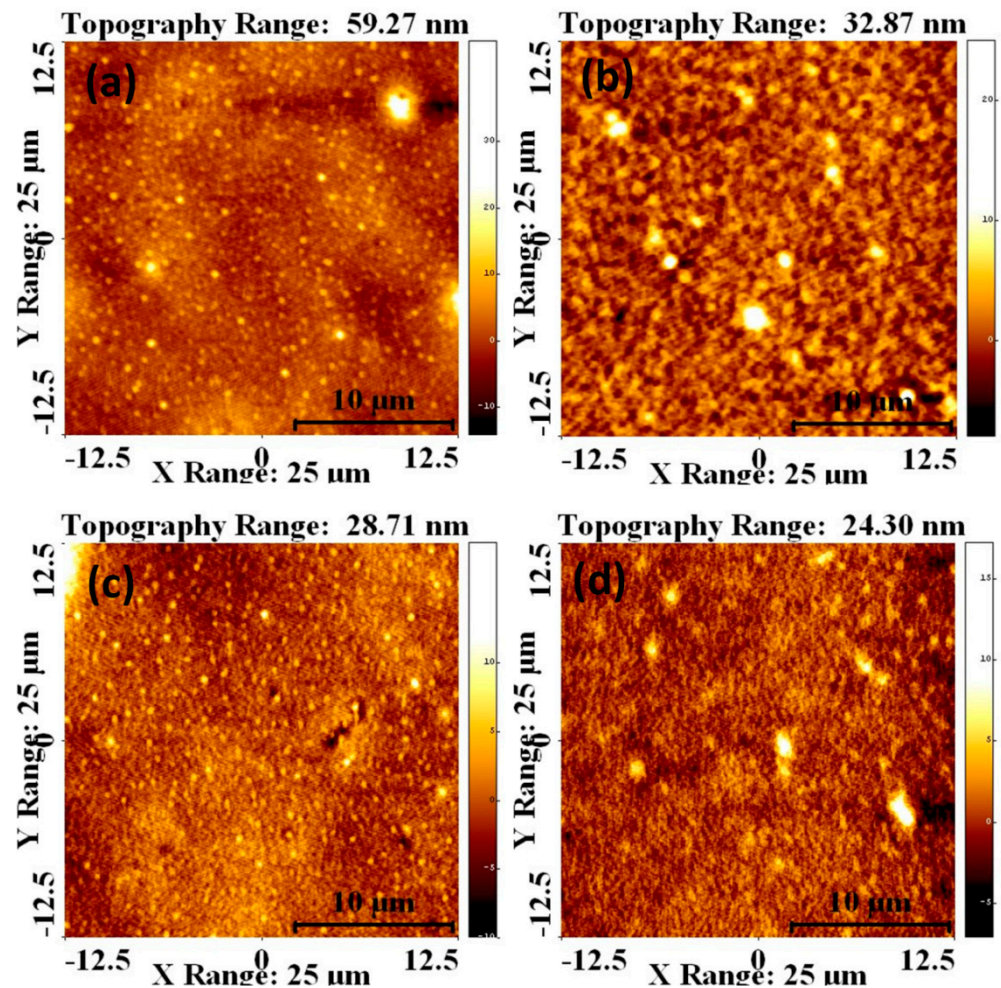

Figure 8. AFM images of the top view of the P$_3$HT:PCBM:Sb$_2$S$_3$ NC blends prepared with Sb$_2$S$_3$ NC concentrations of (**a**) 0.01, (**b**) 0.02, (**c**) 0.03, and (**d**) 0.04 mg/mL.

Figure 9 displays the Fourier transform infrared (FT-IR) spectra recorded in the 250–4000 cm^{-1} spectral regions in the P$_3$HT:PCBM:Sb$_2$S$_3$ NC blended films. In the 2700–3100 cm^{-1} spectral region, the methylene and methyl stretching vibration bands from the hexyl side chains of the thiophene rings were notable. The P$_3$HT polymer exhibited vibration bands at 2954 and 3054 cm^{-1} corresponding to the stretching and asymmetric vibrations of =C-H and C=C [40,41]. The band at 1260 cm^{-1} corresponded to the dipole-derivative vector perpendicular to the ring plane, and the band near 1048 cm^{-1} was due to C-H in-plane bending [42]. The vibration mode at 1454 cm^{-1} was due to the deformation vibrations of the CH and CH$_3$ [41]. The vibration modes in the 1600–1800 cm^{-1} region, such as 1715 cm^{-1}, were due to photo-degradation products, including C=O groups [43]. The vibration mode at 1107 cm^{-1} corresponded to O=S stretching due to sulfonic esters [44]. The band near 820 cm^{-1} was related to the asymmetric deformation of CH3 vibrations (aromatic out-of-plain vibrations) [45]. Finally, the band at 1591cm^{-1} was due to C=C bands [46].
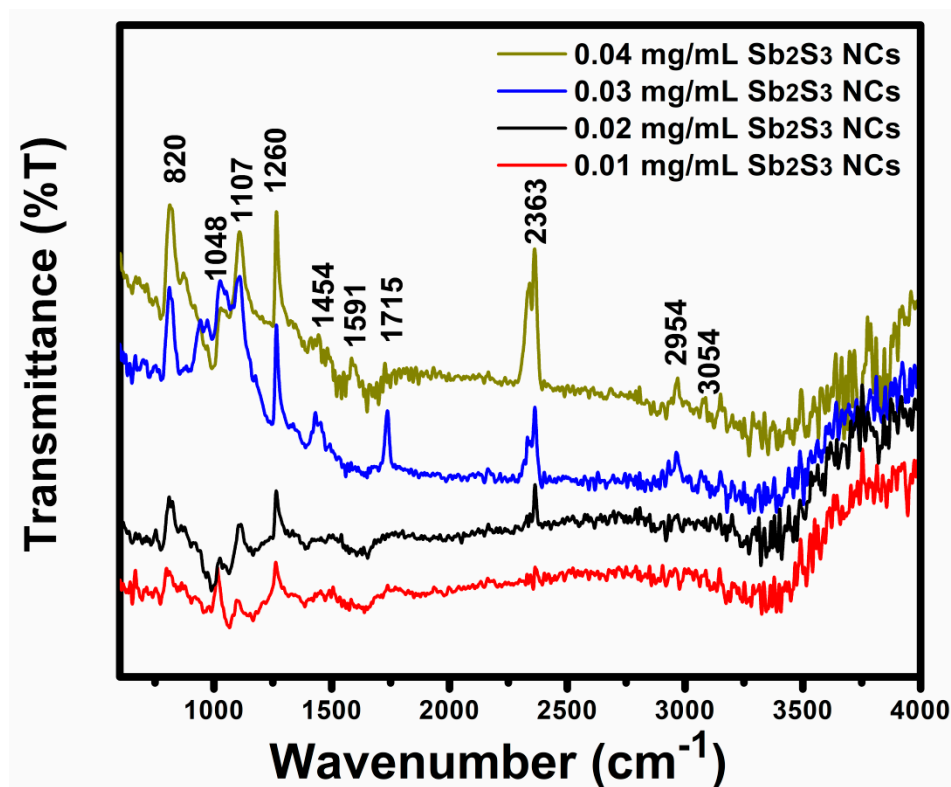
Figure 9. FTIR spectra of the P$_3$HT:PCBM:Sb$_2$S$_3$ NC blended films with different Sb$_2$S$_3$ NC concentrations.

Our results were in good agreement with previous studies of FT-IR vibrations of pristine P$_3$HT:PCBM. Very considerable changes suggested chemical degradation, as demonstrated after doping, leading to an essential increase in the peaks' intensity in the vibration bands at 820, 2954, 2363, and 1260 cm^{-1}, features of the hexyl side chains. This indicated that the hexyl side chains began to separate from the thiophene rings and eventually volatilized. As a result, as the doping concentration increased, the thiophene rings strengthened, affecting the increase in the P$_3$HT band's intensity, with a small shift related to the improved polymer chains leading to the phase separation of the P$_3$HT:PCBM blend. The FT-IR results described the phase separation processes in the blend and vibration modes of the polymer chemical groups.

To evaluate the influence of the Sb$_2$S$_3$ NCs on the performance of theP$_3$HT:PCBM:Sb$_2$S$_3$ NCs'photovoltage, four polymer devices with different concentrations of Sb$_2$S$_3$ NC-doped active layers (displayed in Figure 10) were fabricated. Figure 10 shows the current–voltage (IV) curves of the devices under AM 1.5G simulation and 100 mW/cm^2 illumination. Table 1 summarizes the results of the open-circuit voltage (V$_{oc}$), short-circuit current (I$_{sc}$), fill factor (FF), and solar energy conversion efficiency (η) of the devices obtained with differentSb$_2$S$_3$ NC concentrations. The IV curves display the increases in the photocurrent that corresponded to the presence of theSb$_2$S$_3$ NCs in the active layer. In reference to the doping concentration of the Sb$_2$S$_3$ NCs shown in Table 1, 0.04 mg/mL was the optimum weight concentration that produced the highest efficiency η = 2.72% related to I$_{sc}$ = 10.04 mA/cm^2, V$_{oc}$ = 412 mV, and FF = 66%.

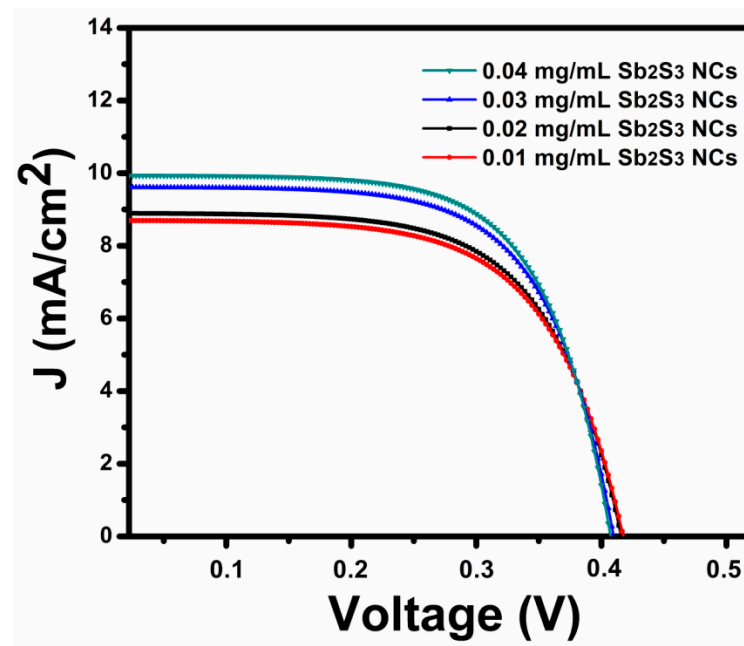**Figure 10.** Current density–voltage (J–V) characteristics of the solar cell device with a glass/ITO/PEDOT:PSS/P$_3$HT:PCBM:Sb$_2$S$_3$:NC/MoO$_3$/Ag configuration.

Table 1. Detailed photovoltaic parameters of the organic solar cell device under AM 1.5 sun illumination with light power intensity of 100 mW/cm^2.

Sample	V$_{oc}$ (mV)	J$_{sc}$ (mA/cm^2)	FF (%)	η (%)	R$_s$ (Ω cm^2)	R$_{sh}$(Ω cm^2)
0.01 mg/mL	423	8.67	59.8	2.18	47.7	489.7
0.02 mg/mL	421	8.91	62.6	2.34	33.6	552.6
0.03 mg/mL	416	9.57	64.4	2.56	26.6	742.1
0.04 mg/mL	412	10.04	66.0	2.72	23.2	945.2

Generally, the increase in the FF and V$_{oc}$ was due to the increase in the R$_{sh}$ and decrease in the R$_s$. The device-resistant reduction was primarily attributed to the improved morphology in the active layer. The significantly increased J$_{sc}$ and FF may have been due to a new network of Sb$_2$S$_3$ NCs that facilitated electron transport in the polymer's active layer and a small range of PCBM aggregation that decreased the carrier recombination losses and increased the current density. In addition, the improved photocurrent corresponded to enhanced entrapment and light absorption, which were demonstrated by an energetic disorder or the improved crystallinity of the P$_3$HT. The increase in the J$_{sc}$ may also have been due to the increased incorporation of the Sb$_2$S$_3$ NCs in the P$_3$HT, which demonstrated that the Sb$_2$S$_3$ NCs could work as electron acceptors comparable to the PCBM, which helped separate the bound photo-generated excitons. The decreases in V$_{oc}$ with a lower concentration of Sb$_2$S$_3$ may be due to the weak interaction that occurs between the polymer and the nanocrystals' interface, which leads to the incomplete charge transfer between the polymer and the nanocrystals, that could decrease the transport of charge-carriers in the hybrid solar cell. This mechanism could have caused many free electrical charges, increased the short-circuit current density, and thus improved the power conversion efficiency. Thus, Sb$_2$S$_3$ NCs blended in a polymer matrix provide a large interfacial area for fast charge dissociation at the interface to ensure that a maximum number of charge carriers contribute to improve the short current density. The performances of fabricated devices can be improved further by incorporating a thin layer of MoO$_3$ as a hole transport layer between the hybrid blend and the back electrodes' Ag.

4. Conclusions

In conclusion, we successfully synthesized highly crystalline Sb_2S_3 NCs using the solvothermal method. We synthesized bulk heterojunction organic solar cells based on $P_3HT:PCBM:Sb_2S_3$ NCs by adding Sb_2S_3 NCs to the active layer. The device's electrical, morphological, and optical properties were significantly affected by the Sb_2S_3 NC concentration in the $P_3HT:PCBM$. The doping concentration improved the surface roughness of the active layer and tapping mode operation. The phase distribution of the blends was also investigated. The high crystalline polymer enhanced the red shift of the optical absorption, increased the photoluminescence intensity, and narrowed the full width at half the maximum of the Raman peaks. The results indicated that the Sb_2S_3 NCs strongly affected the flat-on orientation, which increased the charge carrier transport assisted by the π-π interactions. The increased number of P_3HT single chains and the phase separation increased the free electrons, which effected the absorption and mobility and reduced the charge recombination in the active layer blend prepared using a concentration of 0.04 mg/mL. Our studies suggest that the charge separation and current generation in $P_3HT:PCBM:Sb_2S_3:NC$-based devices result mainly from Sb_2S_3 NCs' light absorption and subsequent hole-transfer from the inorganic semiconductor to the organic hole transporting material. The best power conversion efficiency (PCE) of the polymer solar cells was 2.72%, using a glass/ITO/PEDOT:PSS/$P_3HT:PCBM:Sb_2S_3:NC$/MoO_3/Ag device structure, under AM 1.5 sun, and global irradiation of 1000 W m^{-2} by blending the Sb_2S_3 NCs with a concentration of 0.04 mg/mL in the active layer. An expected mechanism is also proposed to explain the superior performance of Sb_2S_3NC-doped $P_3HT:PCBM$ at optimal content.

References

1. Wang, G.; Adil, M.A.; Zhang, J.; Wei, Z. Large-area organic solar cells: Material requirements, modular designs, and printing methods. *Adv. Mater.* **2019**, *31*, 1805089. [CrossRef]
2. Liu, G.; Jia, J.; Zhang, K.; Jia, X.E.; Yin, Q.; Zhong, W.; Li, L.; Huang, F.; Cao, Y. 15% Efficiency Tandem Organic Solar Cell Based on a Novel Highly Efficient Wide-Bandgap Nonfullerene Acceptor with Low Energy Loss. *Adv. Energy Mater.* **2019**, *9*, 1803657. [CrossRef]
3. Abdallaoui, M.; Sengouga, N.; Chala, A.; Meftah, A.; Meftah, A. Comparative study of conventional and inverted p3ht:Pcbm organic solar cell. *Opt. Mater.* **2020**, *105*, 109916. [CrossRef]
4. Berger, P.; Kim, M. Polymer solar cells: P3ht:Pcbm and beyond. *J. Renew. Sustain. Energy* **2018**, *10*, 013508. [CrossRef]
5. Oklobia, O.; Komilian, S.; Sadat-Shafai, T. Impedance spectroscopy and capacitance–voltage measurements analysis: Impact of charge carrier life times and mapping vertical segregation in bulk heterojunction p3ht:Pcbm solar cells. *Org. Electron.* **2018**, *61*, 276–281. [CrossRef]
6. Hemaprabha, E.; Pandey, U.K.; Chattopadhyay, K.; Ramamurthy, P.C. Doped silicon nanoparticles for enhanced charge transportation inorganic-inorganic hybrid solar cells. *Sol. Energy* **2018**, *173*, 744–751. [CrossRef]
7. Gao, H.; Meng, J.; Sun, J.; Deng, J. Enhanced performance of polymer solar cellsbased on p3ht:Pcbm via incorporating Au nanoparticles prepared by the micellar method. *J. Mater. Sci. Mater. Electron.* **2020**, *31*, 10760–10767. [CrossRef]
8. Mousavi, S.L.; Jamali-Sheini, F.; Sabaeian, M.; Yousefi, R. Enhanced solar cell performance of p3ht:Pcbm by sns nanoparticles. *Sol. Energy* **2020**, *199*, 872–884. [CrossRef]
9. Kondrotas, R.; Chen, C.; Tang, J. Sb2s3 solar cells. *Joule* **2018**, *2*, 857–878. [CrossRef]

10. Yuan, S.; Deng, H.; Yang, X.; Hu, C.; Khan, J.; Ye, W.; Tang, J.; Song, H. Postsurface selenization for high performance sb2s3 planar thin film solar cells. *ACS Photonics* **2017**, *4*, 2862–2870. [CrossRef]

11. Jiang, C.; Tang, R.; Wang, X.; Ju, H.; Chen, G.; Chen, T. Alkali metals doping for high-performance planar heterojunction sb2s3 solar cells. *Sol. RRL* **2019**, *3*, 1800272. [CrossRef]

12. Zhao, Y.; Yang, S.; Zhao, J.; Zou, B. Pbs quantum dots base dorganic-inorganic hybrid infrared detecting and display devices. *Mater. Lett.* **2017**, *196*, 176–178. [CrossRef]

13. Kim, O.; Kwon, J.; Kim, S.; Xu, B.; Seo, K.; Park, C.; Do, W.; Bae, J.; Kang, S. Effect of pvp-capped zno nanoparticles with enhanced charge transport on the performance of p3ht/pcbm polymer solar cells. *Polymers* **2019**, *11*, 1818. [CrossRef]

14. Parize, R.; Cossuet, T.; Chaix-Pluchery, O.; Roussel, H.; Appert, E.; Consonni, V. In situ analysis of the crystallization process of sb2s3 thin films by raman scattering and x-ray diffraction. *Mater. Des.* **2017**, *121*, 1–10. [CrossRef]

15. Medina-Montes, M.; Montiel-González, Z.; Mathews, N.; Mathew, X. The influence of film deposition temperature on the subsequent post-annealing and crystallization of sputtered sb2s3 thin films. *J. Phys. Chem. Solids* **2017**, *111*, 182–189. [CrossRef]

16. Osorio Mayon, Y.; White, T.P.; Wang, R.; Yang, Z.; Catchpole, K.R. Evaporated and solution deposited planar sb2s3 solar cells: A comparison and its significance. *Phys. Status Solidi* **2016**, *213*, 108–113. [CrossRef]

17. Mech, W.; Borysiuk, J.; Wincukiewicz, A.; Bożek, R.; Trautman, P.; Tokarczyk, M.; Kamińska, M.; Korona, K. Influence of active layer processing on electrical properties and efficiency of polymer—Fullerene organic solar cells. *Acta Phys. Pol. A* **2019**, *136*, 579–585. [CrossRef]

18. Siddiqui, H.; Parra, M.R.; Pandey, P.; Qureshi, M.; Haque, F.Z. Combined parametric optimization of p3ht:Pc70bm films for efficient bulk-heterojunction solar cells. *J. Solid State Electrochem.* **2019**, *23*, 3267–3274. [CrossRef]

19. Berriman, G.A.; Holmes, N.P.; Holdsworth, J.L.; Zhou, X.; Belcher, W.J.; Dastoor, P.C. A new model for pcbm phase segregation in p3ht:Pcbm blends. *Org. Electron.* **2016**, *30*, 12–17. [CrossRef]

20. Hwang, S.; Potscavage, W.J., Jr.; Nakamichi, R.; Adachi, C. Processing and doping of thick polymer active layers for flexible organic thermoelectric modules. *Org. Electron.* **2016**, *31*, 31–40. [CrossRef]

21. Untilova, V.; Biskup, T.; Biniek, L.; Vijayakumar, V.; Brinkmann, M. Control of chain alignment and crystallization helps enhance charge conductivities and thermoelectric power factors in sequentially doped p3ht:F4tcnq films. *Macromolecules* **2020**, *53*, 2441–2453. [CrossRef]

22. Chandrasekaran, N.; Kumar, A.; Thomsen, L.; Kabra, D.; McNeill, C.R. High performance as-cast p3ht:Pcbm solar cells: Understanding the role of molecular weight in high regioregularity p3ht. *Mater. Adv.* **2021**, *2*, 2045–2054. [CrossRef]

23. Kumar, S.; Kumar, M.; Rathi, S.; Yadav, A.; Upadhyaya, A.; Gupta, S.K.; Singh, A. Study of p3ht/pcbm Morphology Using Raman Spectroscopy. *AIP Conf. Proc.* **2018**, *1953*, 100074. [CrossRef]

24. Hisamuddin, S.N.; Abdullah, S.M.; Alwi, S.A.K.; Majid, S.R.; Anuar, A.; Sulaiman, K.; Tunmee, S.; Chanlek, N.; Bawazeer, T.M.; Alsoufi, M.S. Optimizing the performance of p3ht-based photodetector by tuning the composition of oxcba. *Synth. Met.* **2020**, *268*, 116506. [CrossRef]

25. Xie, T.; Xie, G.; Su, Y.; Hongfei, D.; Ye, Z.; Jiang, Y. Ammonia gas sensors based on poly(3-hexylthiophene)-molybdenum disulfide film transistors. *Nanotechnology* **2016**, *27*, 065502. [CrossRef] [PubMed]

26. Chang, S.-C.; Hsiao, Y.-J.; Lin, T.-C.; Li, T.-S.; Zeng, S.-A.; Yu, C.-E. Improving power conversion efficiency of p3ht/pcbm based organic solar cells by optimizing graphene doping concentration and annealing temperature. *Int. J. Electrochem. Sci* **2016**, *11*, 5819–5828. [CrossRef]

27. Hamed, Z.B.; Mastour, N.; Kouki, F.; Sanhoury, M.; Bouchriha, H. Franck–condon analysis of fluorescence quenching in hybrid p3ht:Wt% tbpo-capped cdse quantum dot matrix. *J. Lumin.* **2016**, *170*, 30–36. [CrossRef]

28. Kozlov, O.V.; Luponosov, Y.N.; Solodukhin, A.N.; Flament, B.; Douhéret, O.; Viville, P.; Beljonne, D.; Lazzaroni, R.; Cornil, J.; Ponomarenko, S.A. Simple donor-acceptor molecule with long exciton diffusion length for organic photovoltaics. *Org. Electron.* **2018**, *53*, 185–190. [CrossRef]

29. Dinçalp, H.; Saltan, G.M.; Zafer, C.; Kıymaz, D.A. Bromo-substituted cibalackrot backbone, a versatile donor or acceptor main core for organic optoelectronic devices. *J. Mol. Struct.* **2018**, *1173*, 512–520. [CrossRef]

30. Otieno, F.; Mutuma, B.K.; Airo, M.; Ranganathan, K.; Erasmus, R.; Coville, N.; Wamwangi, D. Enhancement of organic photovoltaic device performance via p3ht:Pcbm solution heat treatment. *Thin Solid Film.* **2017**, *625*, 62–69. [CrossRef]

31. Song, C.; Wang, Z.; Li, J.; Chen, Y.; Zhao, F.; Zhang, H. Extension of π-conjugation and enhancement of electron-withdrawing ability at terminal indanedione for a-π-d-π-a small molecules for application in organic solar cells. *Org. Electron.* **2020**, *81*, 105679. [CrossRef]

32. Ahmad, Z.; Touati, F.; Shakoor, R.; Al-Thani, N. Study of a ternary blend system for bulk heterojunction thin film solar cells. *Chin. Phys. B* **2016**, *25*, 080701. [CrossRef]

33. Lefrançois, A.; Luszczynska, B.; Pepin-Donat, B.; Lombard, C.; Bouthinon, B.; Verilhac, J.-M.; Gromova, M.; Faure-Vincent, J.; Pouget, S.; Chandezon, F. Enhanced charge separation in ternary p3ht/pcbm/cuins 2 nanocrystals hybrid solar cells. *Sci. Rep.* **2015**, *5*, 1–8. [CrossRef] [PubMed]

34. Gollu, S.R.; Sharma, R.; Srinivas, G.; Kundu, S.; Gupta, D. Incorporation of silver and gold nanostructures for performance improvement in p3ht:Pcbm inverted solar cell with rgo/zno nanocomposite as an electron transport layer. *Org. Electron.* **2016**, *29*, 79–87. [CrossRef]

35. Oseni, S.O.; Mola, G.T. Bimetallic nanocomposites and the performance of inverted organic solar cell. *Compos. Part B Eng.* **2019**, *172*, 660–665. [CrossRef]

36. Dwivedi, S.K.; Tiwari, D.; Tripathi, S.K.; Dwivedi, P.K.; Dipak, P.; Chandel, T.; Prasad, N.E. Fabrication and properties of p3ht:Pcbm/cu2snse3(ctse) nanocrystals based inverted hybrid solar cells. *Sol. Energy* **2019**, *187*, 167–174. [CrossRef]

37. Qu, S.; Yao, Q.; Wang, L.; Chen, Z.; Xu, K.; Zeng, H.; Shi, W.; Zhang, T.; Uher, C.; Chen, L. Highly anisotropic p3ht films with enhanced thermoelectric performance via organic small molecule epitaxy. *NPG Asia Mater.* **2016**, *8*, e292. [CrossRef]

38. Aoyama, Y.; Douhéret, O.; Leclère, P.; Moerman, D.; Mizukado, J.; Suda, H.; Lazzaroni, R.; Yoshida, Y. On the influence of the photo-oxidation of p3ht on the conductivity of photoactive film of p3ht:Pcbm bulk heterojunctions. *Org. Electron.* **2017**, *43*, 142–147. [CrossRef]

39. Corzo, D.; Almasabi, K.; Bihar, E.; Macphee, S.; Rosas-Villalva, D.; Gasparini, N.; Inal, S.; Baran, D. Digital inkjet printing of high-efficiency large-area nonfullerene organic solar cells. *Adv. Mater. Technol.* **2019**, *4*, 1900040. [CrossRef]

40. Hernández-Martínez, D.; Nicho, M.; Alvarado-Tenorio, G.; García-Carvajal, S.; Castillo-Ortega, M.; Vásquez-López, C. Elaboration and characterization of p3ht–peo–swcnt fibers by electrospinning technique. *SN Appl. Sci.* **2020**, *2*, 1–9. [CrossRef]

41. Brambilla, L.; CapelFerrón, C.; Tommasini, M.; Hong, K.; López Navarrete, J.; Hernández, V.; Zerbi, G. Infrared and multi-wavelength raman spectroscopy of regio-regular p3ht and its deuteron derivatives. *J. Raman Spectrosc.* **2018**, *49*, 569–580. [CrossRef]

42. de Antoni, L.O.; de Menezes, E.W.; Loguercio, L.F.; Rodrigues, M.R.F.; de Andrade, R.L.; Costa, T.M.; Benvenutti, E.V.; Santos, J.F.L.; Santos, M.J.L. Ionic silsesquioxane-capped au nanoparticle powders: Application in p3ht/pcbm solar cells and the effect of the capping layer on surface plasmon dumping. *Mater. Chem. Phys.* **2018**, *206*, 204–212. [CrossRef]

43. Agbolaghi, S. Optical/thermal studies on nanostructures of poly(3-hexylthiophene) and carbon nanotube/graphene precursors. *Fuller. Nanotub. Carbon Nanostruct.* **2019**, *27*, 572–581. [CrossRef]

44. Sharma, T.; Singhal, R.; Vishnoi, R.; Sharma, P.; Patra, A.; Chand, S.; Lakshmi, G.; Biswas, S. Electronic excitation induced modifications of optical and morphological properties of pcbm thin films. *Nucl. Instrum. Methods Phys. Res. Sect. B Beam Interact. Mater. At.* **2016**, *379*, 176–180. [CrossRef]

45. Subhashini, R.; Sathya, D.; Sivashankar, V.; Mageshwari, P.L.; Arjunan, S. Growth and characterization of bis(l-threonine) copper (ii) monohydrate single crystals: A semiorganic second order nonlinear optical material. *Opt. Mater.* **2016**, *62*, 357–365. [CrossRef]

46. Sakthiguru, N.; Sithique, M.A. Preparation and in vitro biological evaluation of lawsone loaded o-carboxymethyl chitosan/zinc oxide nanocomposite for wound-healing application. *Chem. Sel.* **2020**, *5*, 2710–2718. [CrossRef]